Geophysical Research Letters

RESEARCH LETTER
10.1029/2019GL085670

The Life Cycle of Annual Waves in the Indian Ocean as Identified by Seamless Diagnosis of the Energy Flux

Zimeng Li[1] and Hidenori Aiki[2,3]

[1]Graduate School of Environmental Studies, Nagoya University, Nagoya, Japan, [2]Institute for Space-Earth Environmental Research, Nagoya University, Nagoya, Japan, [3]Application Laboratory, Japan Agency for Marine-Earth Science and Technology, Yokohama, Japan

Key Points:
- The horizontal transfer routes of annual wave energy in the tropical Indian Ocean are identified by using a shallow-water equation model
- Localized cyclonic circulation of wave energy along African coasts is detected in both hemispheres
- An eastward energy flux at the equator appears at both eastward and westward peak times of zonal wind anomaly in the central Indian Ocean

Supporting Information:
- Supporting Information S1

Correspondence to:
Z. Li and H. Aiki,
lizimeng1995@gmail.com;
aiki@nagoya-u.jp

Citation:
Li, Z., & Aiki, H. (2020). The life cycle of annual waves in the Indian Ocean as identified by seamless diagnosis of the energy flux. *Geophysical Research Letters*, *47*, e2019GL085670. https://doi.org/10.1029/2019GL085670

Received 31 OCT 2019
Accepted 30 DEC 2019
Accepted article online 3 JAN 2020

Abstract In previous studies, the role of large-scale waves in tropical-extratropical interactions has been little investigated in terms of wave energy transfer owing to the lack of appropriate diagnostic techniques. Using a new seamless scheme, the present study identifies a series of well-defined horizontal circulation routes of wave energy in the Indian Ocean on an annual basis. One of these features represents a localized cyclonic circulation close to the western boundary in each hemisphere while the other manifests as a basin-scale cyclonic circulation in the eastern Indian Ocean. For the second baroclinic mode, eastward energy fluxes associated with equatorial Kelvin waves appear when zonal velocity anomaly exhibits eastward and westward peaks (four times per year) in response to the monsoon-wind cycle. Identification of these key pathways of wave energy circulation enables us to better understand how waves in the tropical and subtropical regions interconnect at the zonal boundaries of the Indian Ocean.

Plain Language Summary By using a new seamless scheme Aiki et al. (2017, https://doi.org/10.1186/s40645-017-0121-1), we provide a groundbreaking view of the life cycle of annual waves in the Indian Ocean from the perspective of wave energetics. Based on an analysis of group velocity vectors, the present study quantifies the significance of the transfer routes of wave energy with a smooth transition between the tropical and subtropical regions. The well-defined circulation routes of wave energy demonstrate that Kelvin waves and Rossby waves interconnect at the zonal boundaries of the Indian Ocean. We identify two sets of cyclonic circulations of wave energy in each hemisphere based on an annual mean analysis: The first of these represents a localized cyclonic circulation close to the African coasts, while the other is a large-scale cyclonic circulation in the eastern side of the basin. The new scheme reveals eastward energy fluxes of equatorial Kelvin waves in the second baroclinic mode at the equator. These eastward energy fluxes appear when zonal velocity anomaly exhibits eastward and westward peaks (four times per year). The present brief contribution opens up a new research theme in the study of wave energy fluxes and their potential role in influencing climate variations.

1. Introduction

Significant annual and semiannual variations in currents and large-scale waves take place in the Indian Ocean (IO). At the equator, westerly winds in spring and autumn cause the semiannual appearance of a Wyrtki (1973) jet as well as equatorial Kelvin waves (KWs), which propagate eastward (Schott & McCreary, 2001, hereafter SM01). The strong westerly winds have a decisive effect on the development and termination of IO Dipole events (Rao & Yamagata, 2004; Saji et al., 1999). Further south, trade winds are persistent in regions around 10°S, while transient signals of heat content associated with westward propagating Rossby waves (RWs) are often found in the southern IO (at latitudes of 8–15°S), which may be partly attributed to wind forcing in the Pacific Ocean during El Niño–Southern Oscillation events (Huang & Kinter, 2002; Ummenhofer et al., 2017).

In the IO, annual and semiannual oscillations and also climate variations are closely linked to the propagation of KWs and RWs (Mark & Huang, 2004; Rahul et al., 2004; Rao et al., 2010). As a packet of oceanic equatorial KWs strikes the eastern boundary, it is refracted backward and is also deflected poleward and becomes the source of both equatorial and midlatitude RWs, which then propagate westward along the flanks of the equator (McPhaden, 1990; Ogata et al., 2017; Schopf et al., 1981; Yu et al., 1991). Wave reflection and diffraction at the zonal boundaries of the IO induce interactions between tropical and subtropical regions. It is

therefore important to investigate how these waves are linked to each other and where they originate from, without subdividing the description in order to reflect the differences in dynamics between the tropical and subtropical regions (Fukutomi & Yasunari, 2002). This issue is explained in the next paragraph.

The aim of the present study is to clarify the mechanical links between the various wave constituents of the IO. At least three existing schemes based on group velocity analysis are in use for diagnosing the geographical routes along which wave energy is transferred (note that these schemes do not rely on Fourier analysis or on ray theory, explained later in the manuscript). The pressure-flux scheme can be used for inertia-gravity waves (Cummins & Oey, 1997), the quasi-geostrophic scheme can be used for midlatitude RWs (Orlanski & Sheldon, 1993, hereafter OS93) though not for equatorial waves or for coastal regions, while Aiki et al. (2017, hereafter abbreviated as AGC17) have developed a diagnostic scheme that tracks the movement of wave energy at all latitudes while satisfying coastal boundary conditions. The latter represents a powerful new tool for understanding the life cycle (generation, propagation, and dissipation process) of disturbance energy in the atmosphere and ocean and is applicable generally rather than to a specific range of latitudes (Ogata & Aiki, 2019).

This study represents the first application of the seamless AGC17 scheme and forms part of a comprehensive investigation of the transfer routes of wave energy in the IO. This initial paper will focus primarily on the seasonal variations. Results from an investigation of interannual variations will be presented in a future study. This manuscript is organized as follows. In section 2, we carry out a set of numerical experiments using a shallow-water equation model associated with the fundamental baroclinic modes that are forced by climatological monsoon winds in the IO. We analyze the transfer routes of wave energy in the IO in section 3 and summarize our results in section 4.

2. Materials and Methods

2.1. Preliminary Analysis

Using the vertical profiles of annual mean salinity and temperature given in the World Ocean Atlas, we have estimated the gravity wave speed $c^{(n)}$ for the nth baroclinic mode in the tropical IO (20°S to 20°N, 40–110°E) based on the bottom-pressure decoupling theory of Tailleux and McWilliams (2001). This eigenvalue problem yields 2.99, 1.69, and 1.03 m/s for the first, second, and third baroclinic mode, respectively (see Table S1 in the supporting information for the corresponding values of equatorial deformation radius and equatorial inertial period). To travel back and forth through a zonal distance L of the IO at the equator (from 45–100°E) takes 0.26, 0.46, and 0.75 years (hereafter referred to as basin mode periods) for the first, second, and third baroclinic mode, respectively. These periods have been estimated as $L/c^{(n)}+3L/c^{(n)}$, on the understanding that the phase speeds of equatorial KWs and long equatorial RWs are written as $c^{(n)}$ (eastward) and $c^{(n)}/3$ (westward), respectively. It is well known that, given the basin mode period of about half a year, the second baroclinic mode is best suited to show the response of the tropical IO to semiannual wind forcing.

2.2. Model Setup

We have performed a set of 20-year climatological experiments associated with the three fundamental baroclinic modes. The model has been discretized in a spherical coordinate system with a grid spacing of (1/4)° in both zonal and meridional directions. The model domain extends from 35–120°E and from 25°S to 20°N and adopts realistic coastlines except for the lack of connection to the Southern Ocean and the Pacific Ocean. For simplicity, all equations in the present manuscript are written in Cartesian coordinates with positive x and y representing the eastward and northward directions. We have used a shallow-water equation model that has been written for the development of zonal velocity $u^{(n)}$, meridional velocity $v^{(n)}$, and geopotential $p^{(n)}$ for the nth baroclinic mode as

$$u_t^{(n)} - fv^{(n)} + p_x^{(n)} = \alpha^{(n)} \frac{\tau_{wind}^x}{\rho_0 \sqrt{H_{mix} H_{bottom}}} + SGS^x, \tag{1a}$$

$$v_t^{(n)} + fu^{(n)} + p_y^{(n)} = \alpha^{(n)} \frac{\tau_{wind}^y}{\rho_0 \sqrt{H_{mix} H_{bottom}}} + SGS^y, \tag{1b}$$

$$p_t^{(n)} + \left(c^{(n)}\right)^2 \left(u_x^{(n)} + v_y^{(n)}\right) = 0, \tag{1c}$$

where subscripts x, y, and t represent partial derivatives associated with the horizontal coordinates and time. Wind stress vector has been calculated by two steps as follows. First we have applied the bulk formula of Large and Pond (1981) to 10-m wind velocity in the European Centre for Medium-Range Weather Forecasts Re-analysis data on 2.5 × 2.5° grids. Here we have used the absolute wind velocity rather than the relative wind velocity (i.e., the difference of the wind velocity and oceanic surface velocity) to calculate the wind stress vector for simplicity. Then we have computed the monthly climatology of wind stress vector and subtracted a climatological annual mean component over the long-term from 1957 to 2002. Thus, the wind stress $\left(\tau_{wind}^x, \tau_{wind}^y\right)$ in the present study represents the seasonal anomaly component of monthly climatology between 1957 and 2002. Use of the seasonal anomaly while excluding the annual mean enables us to focus on the climatological annual and semiannual variations of waves related to the monsoon in the IO. Further important influences from both wave-mean flow interactions and interannual variability will be addressed in a later study.

Wind-induced momentum input to the mixed layer is partitioned into each baroclinic mode and has been estimated here by a nondimensional parameter $\alpha^{(n)} = 0.35$, 0.44, and 0.27 in (1a) and (1b) for the first, second, and third baroclinic modes, respectively (see Appendix A for details); $\rho_0 = 1027$ kg/m^3 in (1a) and (1b) is the reference density of seawater, $H_{mix} = 35.0$ m is the annual mean value of the mixed-layer depth based on a temperature difference of 0.2 °C (as estimated from Argo data gathered in the tropical IO), and $H_{bottom} =$ 5,500 m is the reference value of water depth in the tropical IO. The subgrid-scale (SGS) terms in (1a) and (1b) represent the effect of lateral eddy viscosity based on the Smagorinsky et al. (1965) scheme and use a nondimensional coefficient of 0.1 after squaring. We have performed a total of three experiments for the three fundamental baroclinic modes, each of which has been integrated for 20 years, including spin-up from the state of no motion. We have confirmed that a climatologically equilibrium state has been reached (not shown) in the course of the model integration of each experiment, for which all 100 snapshots (with an output interval of 3.65 days) during the last year are used in the following overall analysis.

2.3. Basic Results

We first present a brief overview of the results of our numerical experiments in order to understand how they reproduce or differ from the actual variations taking place in the IO. Figure 1 shows a set of Hovmöller diagrams at the equator for all three baroclinic modes. The Wyrtki jets are simulated in the second baroclinic mode (Figures S2c and S2g in the supporting information) as shown by the time evolution of zonal velocity, with eastward wind forcing peaks present in both April–June and October–December (contours in the left panels of Figure 1) (Gent et al., 1983; Nagura & McPhaden, 2010). The second baroclinic mode has a basin mode period of 0.46 years (Table S1) and so is able to respond to the semiannual wind forcing at the equator. While the time evolution of zonal velocity shows more westward propagating signals at the equator (color shading in the left panels of Figure 1), the time evolution of the geopotential anomaly shows some of eastward propagating signals at the equator (color shading in the right panels of Figure 1). The significance of simulated Yanai waves (also known as mixed Rossby-gravity waves) (Yanai & Maruyama, 1966) may be verified by looking at the time evolution of the meridional velocity (contours in the right panels of Figure 1) in which these waves are shown to be less relevant than RWs and KWs in the equatorial region of our model experiments. Hereafter, our explanation focuses on either KWs or RWs. See Appendix B and Figure S2 for additional explanation of the basic model results.

3. Results and Discussion

We have analyzed the directionality of wave group velocity vectors in order to understand the transfer routes of wave energy throughout the IO. Figure 2 shows energy flux vectors associated with the second baroclinic mode (left panels), and the third baroclinic mode (right panels), all of which have been calculated by applying an annual average to all 100 snapshots during the twentieth year of model integrations. This figure allows us to compare the performance of the pressure-flux scheme, the OS93 scheme, and the AGC17 scheme (see Appendix C for details). The pressure-flux scheme (Figures 2a and 2b) does not show the westward transfers of wave energy associated with midlatitude RWs, while the OS93 scheme (Figures 2c and 2d) cannot reveal energy fluxes in the vicinities of the equator or coastlines. In contrast, the AGC17 scheme (Figures 2e and 2f)

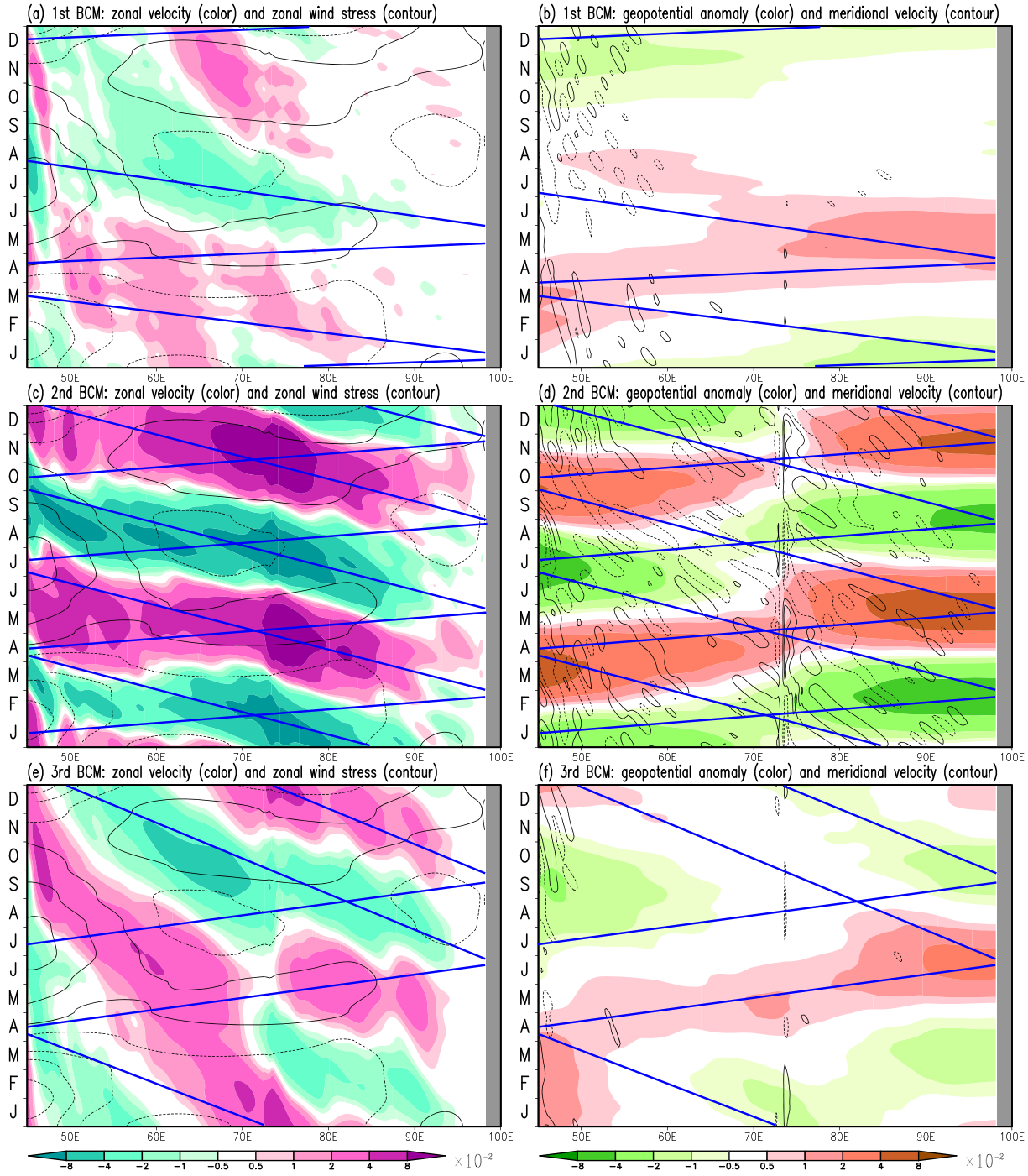

Figure 1. Hovmöller diagrams at the equator for the results of model experiments associated with (a, b) the first baroclinic mode, (c, d) the second baroclinic mode, and (e, f) the third baroclinic mode. Left panels (a, c, and e): the zonal component of simulated velocity (color shading with a unit of meters per second) and the zonal component of wind stress (solid and dotted contours for positive and negative values, respectively, with an interval of 0.01 N/m^2) as the part of the model forcing. Right panels (b, d, and f): simulated geopotential anomaly (color shading with a unit of meters per second, rescaled as $p^{(n)}/c^{(n)}$ to follow the definition of gravitational potential energy) and the meridional component of simulated velocity (solid and dotted contours represent positive and negative values, respectively, with an interval of 0.02 m/s). Solid blue lines indicate the theoretical phase speeds of both Kelvin waves and equatorial long Rossby waves for each baroclinic mode.

is able to show both westward energy fluxes associated with midlatitude RWs and eastward energy fluxes associated with equatorial KWs. The AGC17 scheme is also able to identify the equatorward energy fluxes along the coastlines of the African continent. Contours in Figure 2 show an annual mean input of wave

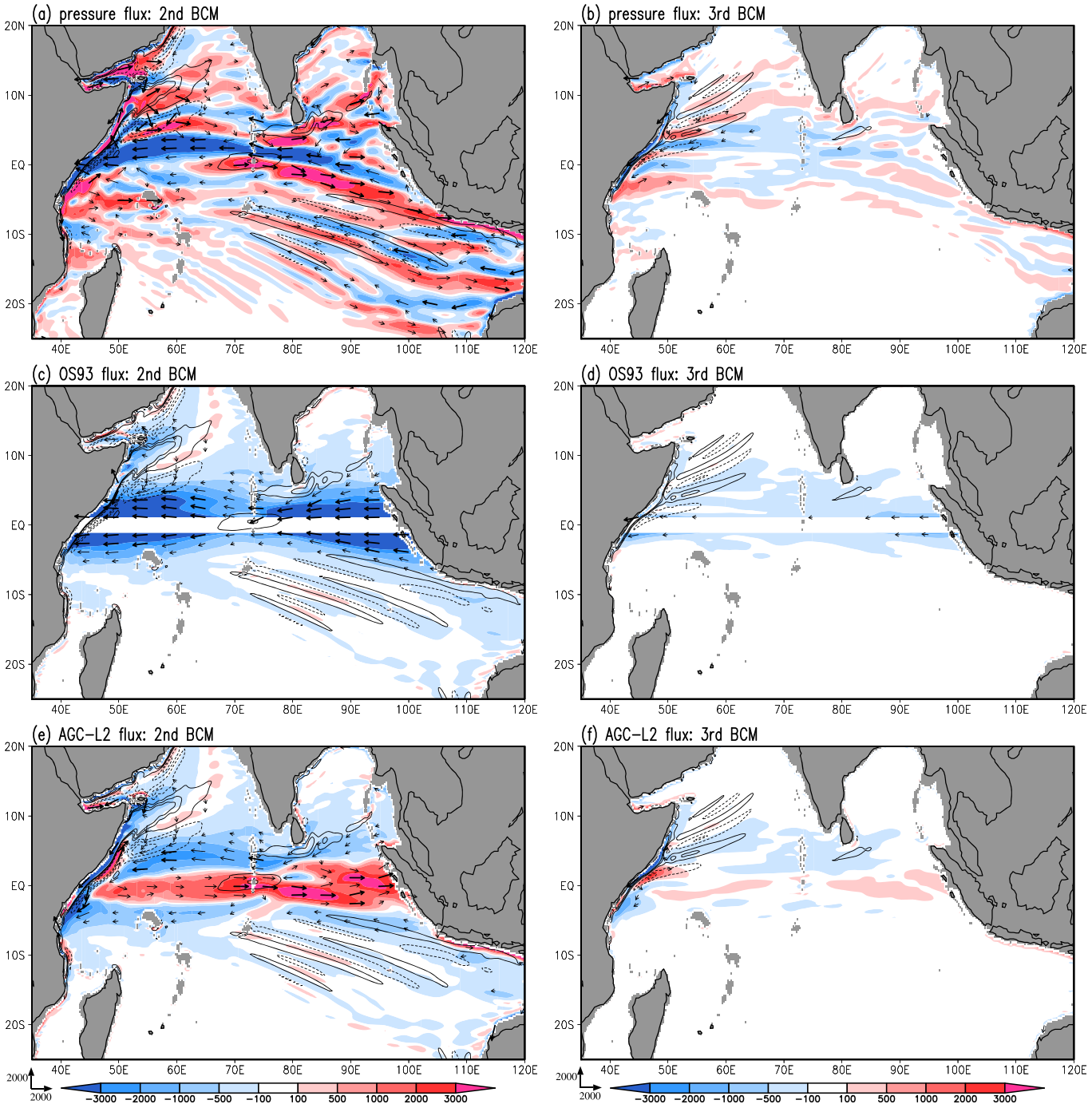

Figure 2. Arrows: energy flux vectors estimated using (a, b) the pressure flux scheme, (c, d) the Orlanski and Sheldon scheme, and (e, f) the AGC17 scheme (Level-2) with magnitude indicated by either the length of arrows (for ranges less than 2,000 W/m) or thick arrows with a constant length (for greater ranges). Left panels (a, c, and e): the second baroclinic mode. Right panels (b, d, and f): the third baroclinic mode. Color shading shows the zonal component of energy flux with a unit of watts per meter. Contours indicate wave energy input by wind forcing (solid and dotted contours for positive and negative values, respectively, with an interval of 0.002 W/m^2). All quantities in all panels have been calculated using an annual average.

energy by wind forcing (see Appendix C, which includes an explanation of the specific mathematical expression). The wind input has a positive peak north of the equator at around 85°E in both second and third baroclinic modes (see contours in Figure 2). This result indicates that midlatitude RWs in this region are revived by local wind forcing. The wind input shows alternating signals in the other regions, owing to

the phase relationship between waves and annual forcing. Further details of the wind input are provided later in the manuscript.

Based on this annual mean analysis (Figures 3a and 3b), our results suggest the presence of two sets of cyclonic circulations of wave energy in each hemisphere (green arrows in Figure 3c). These are listed as follows:

- Localized cyclonic circulation close to the African coasts.
- Large-scale cyclonic circulation in the eastern side of the basin.

Near the western boundary of the IO, the seasonal variations of both the Somali Current (SC) and the East African Coastal Current (EACC) generate equatorward energy fluxes along the African coasts, forming a localized cyclonic energy circulation in each hemisphere. Identification of this energy circulation has been facilitated by the fact that the AGC17 scheme has the advantage of satisfying the coastal boundary conditions. Thus, the AGC17 scheme generates no energy flux in the direction normal to model coastlines, which stands in contrast to the OS93 scheme. The net equatorward transports of wave energy at the western boundary of the IO in the northern and southern hemispheres have been estimated as −3.59 and 2.07 GW (gigawatts), respectively. As equatorial KWs arrive at the eastern boundary, they bifurcate poleward along the coasts of the Indonesian Peninsula and Islands and then radiate midlatitude RWs to form a basin-scale cyclonic circulation of wave energy in each hemisphere (Figures 3a–3c). The net transports of wave energy bifurcating northward and southward at the eastern boundary of the IO have been estimated as −0.87 and 0.96 GW, respectively. These values indicate that about 1/3 ($\approx (0.87 + 0.96)/(3.59 + 2.07)$) of the wave power from the western boundary continues eastward across the zonal extent of the IO at the equator. The northward branch at the eastern boundary reaches the Andaman Sea and then turns westward into the Bay of Bengal, while the southward branch at the eastern boundary reaches the coasts of Australia, and then turns northwestward into the southern IO. The distribution of the energy flux divergence (color shading in Figure 3d) shows meridionally alternating signals that correspond to the distribution of wave energy input by wind forcing (Figure 3e). The energy flux divergence is nearly zero in the eastern equatorial regions (Figure 3d), indicating that KW energy is transferred poleward rather than dissipated locally. Indeed, energy dissipation is significant near the western boundaries where the horizontal scale of the disturbances is relatively small, owing to the presence of coastal currents (Figure 3f). The details of these issues will be investigated in a future study based on both regional statistics and model intercomparisons.

The eastward energy fluxes along the equator in Figure 2 are attributed to equatorial KWs. These warrant further investigation because eastward propagating signals are less pronounced in both the Hovmöller diagrams of zonal velocity and geopotential anomaly (i.e., raw quantities from the model output) in Figure 1. We have computed the energy quantities without a time average to analyze the time evolution of energy flux at the equator and at 5°N, as shown in Figure 4. The AGC17 scheme can identify the eastward transfers of wave energy that are consistent with the group velocity of equatorial KWs (see solid blue lines in Figure 4). In relation to the seasonal evolution in the second baroclinic mode (Figure 4c), eastward signals are found to culminate (four times per year with a maximum in April–May) when zonal velocity exhibits eastward and westward peaks as dictated by the monsoon winds. The timings of wind input at the equators (see contours in Figure 4c) are such as to intensify the eastward energy fluxes associated with equatorial KWs in the central basin. Signals indicating eastward energy fluxes are found to span the full zonal extent of the tropical IO, which may be traced back to the reflection of RWs at the western boundary. For the first and third baroclinic modes, eastward signals can be recognized in the eastern and western regions of the basin, respectively. In the western basin, all three baroclinic modes indicate wave energy input by wind forcing, with semiannual peaks that are attributed to the influence of the monsoon. This wind forcing near the African coast modulates strengths among four KW beams in a year.

Likewise, when used without a time average, the AGC17 scheme can identify the westward transfers of wave energy that are consistent with the group velocity of both long equatorial RWs (see solid blue lines in the left panels of Figure 4) and midlatitude/off-equatorial RWs (the right panels of Figure 4). Overall, the westward energy fluxes (appearing four times per year) are less powerful than the eastward energy fluxes. Equatorial RWs in the western basin originate from wind input in the central basin. Namely, wind input at the equator induces both KWs and RWs at the same time. The fact is that KWs reflected from the western boundary arrive at the central basin at times of wind input is explained by the basin mode period of about half a year in the second baroclinic mode. Figure 4 clearly resolves both wave reflection at the western boundary and

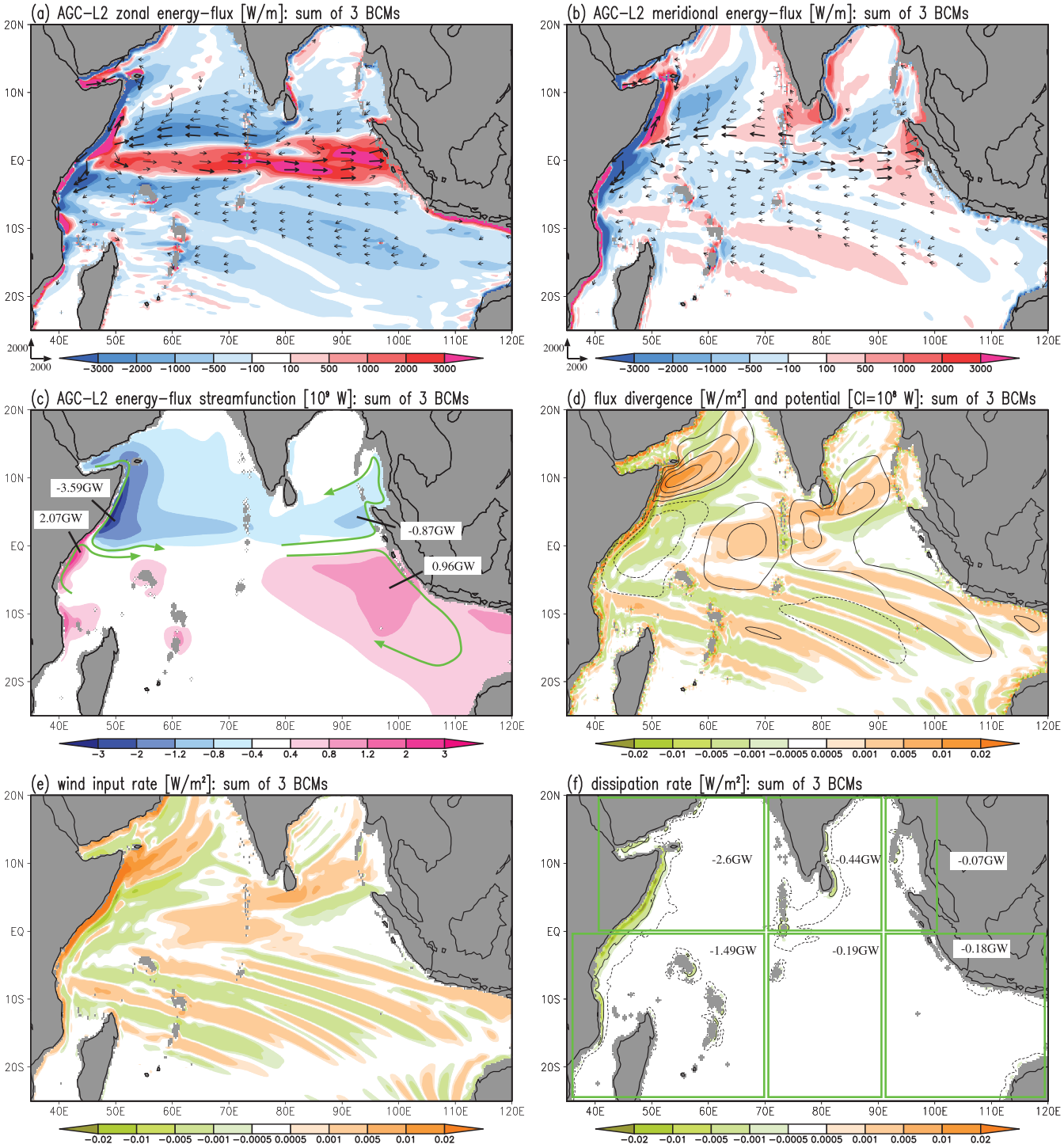

Figure 3. Energy quantities based on an annual average and the sum of fundamental three baroclinic modes. (a) Energy flux vectors with magnitude indicated by either the length of arrows (for ranges less than 2,000 W/m) or thick arrows with a constant length (for greater ranges) and the zonal component of the energy flux (color shading with a unit of watts per meter) that have been estimated using the AGC17 scheme (Level-2). (b) Same as (a) except for color shading showing the meridional component of the energy flux. (c) Energy-flux stream function R (color shading with a unit of 10^9 W = 1 GW), with four numbers indicating locally peak values. Green arrows in (c) represent schematic illustrations for the cyclonic circulations of wave energy in each hemisphere. (d) Energy flux divergence and energy flux potential D (solid and dotted contours for positive and negative values, respectively, with an interval of 10^8 W = 0.1 GW), (e) energy input rate by wind forcing calculated from equation (12c), and (f) energy dissipation rate calculated from equation (12i) (color shading with a unit of watts per square meter). Solid and dotted contours in (f) indicate dissipation rates of $-10^{-3}$and -10^{-4} W/m^2, respectively. Spatially integrated values of the dissipation rate are noted for the boxed subdomains in (f).

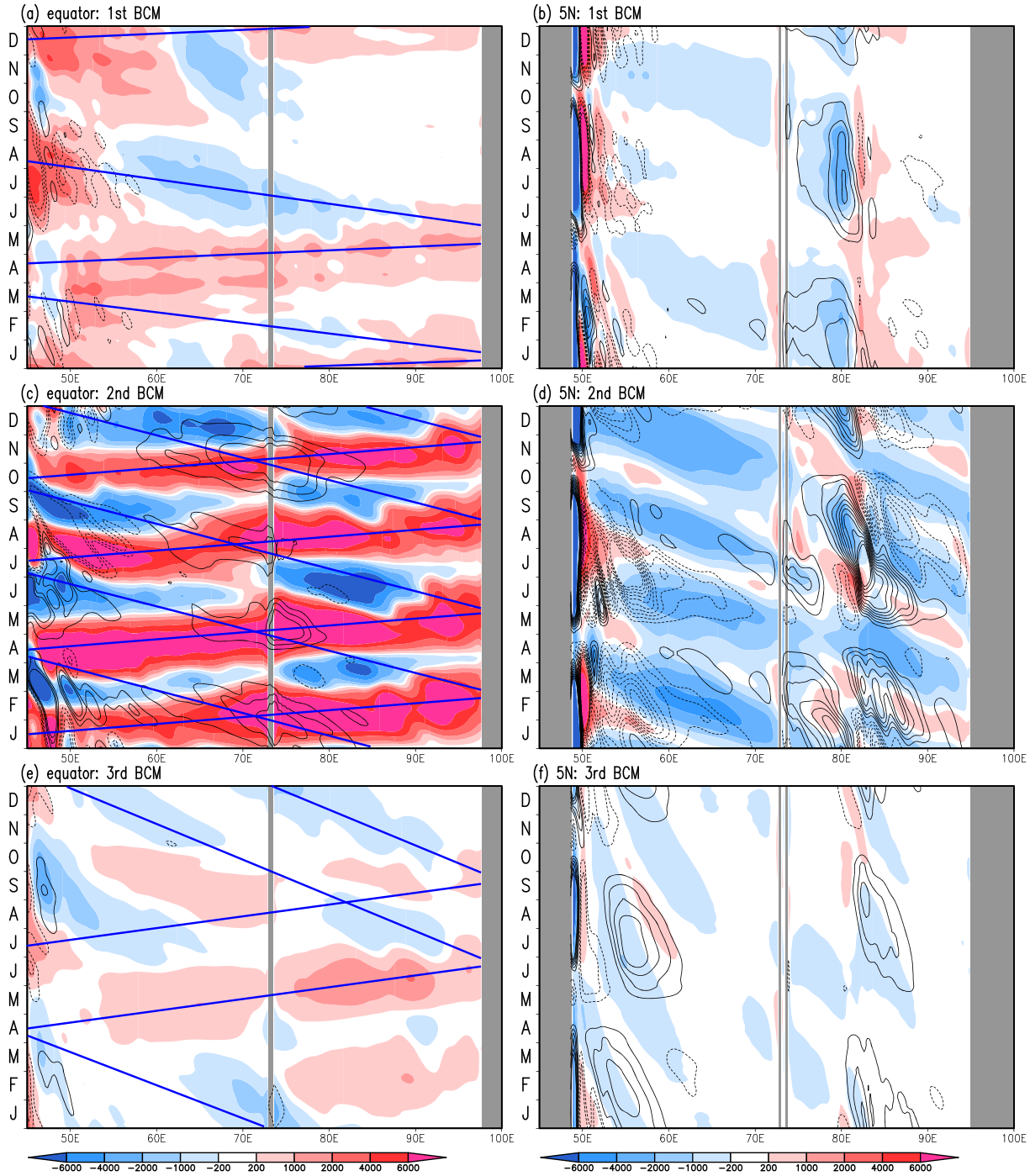

Figure 4. Hovmöller diagrams at the equator (left panels) and at 5°N (right panels) for the results of model experiments associated with (a, b) the first baroclinic mode, (c, d) the second baroclinic mode, and (e, f) the third baroclinic mode. Color shading shows the zonal component of the energy flux (color shading with a unit of watts per meter) computed using the AGC17 scheme (Level-2) without a time average. Solid blue lines in the left panels indicate the theoretical phase speeds of both Kelvin waves and equatorial long Rossby waves for each baroclinic mode. Contours show energy input by wind forcing (solid and dotted contours for positive and negative values, respectively, with an interval of 0.002 W/m^2).

wave diffraction at the eastern boundary. The wind input at 5°N (contours in Figure 4d) is more significant than at the equator (contours in Figure 4c) in the central basin, the former of which corresponds to the wind input peak surrounding the Maldives (from 60°E to 80°E) in the horizontal distribution based on an annual average (color shading in Figure 3e). The presence of wind input in this region may be confirmed by positive

signals in the energy flux potential (contours in Figure 3d). These results illustrate how oceanic waves are linked to each other and where these waves originate from. Reflection and diffraction at the zonal boundaries yield the cyclonic circulations of wave energy in each hemisphere, and in turn these lead to tropical-extratropical exchanges of wave energy.

4. Conclusions

The exchange of wave energy in tropical-extratropical regions has so far remained poorly understood owing to the lack of appropriate diagnostic techniques. The present study has compared three diagnostic schemes to identify the transfer routes of wave energy that theoretically follow group velocity vectors. The pressure-flux scheme cannot represent the westward energy flux of midlatitude RWs, the quasi-geostrophic scheme can be used for midlatitude RWs though not for equatorial KWs or coastal regions. Only the Aiki et al. (2017, hereafter AGC17) scheme has enabled a unified treatment of RWs and KWs and thus allowed us to determine the horizontal transfer routes of wave energy with a smooth transition between tropical and subtropical regions. We conclude that the AGC17 scheme is the most appropriate for tracing the processes of reflection and diffraction of all waves and at all latitudes, while also satisfying the coastal boundary conditions.

This is the first time that the new seamless diagnostic scheme for tracing wave energy fluxes has been used to investigate realistic circulations and waves in the IO. We have focused here on the well-defined seasonal variations associated with the monsoon and performed a set of shallow-water model experiments using climatological wind forcing. In the Hovmöller diagrams of both zonal velocity and geopotential anomaly at the equator (Figure 1), eastward signals related to KWs are less pronounced while westward signals related to RWs are clearly revealed. Near the western boundary of the IO, the seasonal variations of both the Somali jet and EACC are found to generate equatorward energy fluxes along the African coasts, forming a previously undetermined localized cyclonic energy circulation in each hemisphere. About one third of this western boundary wave power continues eastward across the zonal extent of the IO at the equator. Near the eastern boundary of the IO, the incoming signals of equatorial KWs bifurcate poleward along the coasts of the Indonesian Peninsula and Islands and then transmit mid-latitude RWs, forming a basin-scale cyclonic energy circulation in each hemisphere. Application of the AGC17 scheme without a time average yields eastward transfers of wave energy associated with KWs that are consistent with the theoretical value of group velocity. Interestingly, the eastward energy fluxes of equatorial KWs appear when zonal current anomalies exhibit eastward and westward peaks (four times per year in response to the cycle of the monsoon winds) with a maximum in April–May. The details of these issues will be investigated in a future study based on both regional statistics and model intercomparisons. For example, the impact of the Indonesian Throughflow on wave energetics presents an important challenge for the future. Our analysis of annual and semiannual waves provides a basis for a future investigation of waves that vary on interannual timescales and so should lead to a better understanding of tropical-extratropical interactions during, for example, periods when the IO Dipole is active. Such research themes/topics have a direct relevance to the issue of climate variation.

Appendix A: The Definition of Nondimensional Parameter $\alpha^{(n)}$

The nondimensional parameter $\alpha^{(n)}$ in (1a) and (1b) in the main manuscript represents the ratio of wind-induced momentum input to the nth baroclinic mode. For simplicity, here we assume a horizontally uniform ocean and let $u = u(z,t)$ and $v = v(z,t)$ be the zonal and meridional components of velocity, respectively. The tendency term and the turbulent mixing term in the horizontal component of momentum equations may be written as

$$\rho_0 \partial_t u + \cdots = \cdots + \partial_z\left(\tau^x_{turb}\right), \tag{2a}$$

$$\rho_0 \partial_t v + \cdots = \cdots + \partial_z\left(\tau^y_{turb}\right), \tag{2b}$$

where ρ_0 is the reference density of seawater. The symbols $\tau^x_{turb} = \tau^x_{turb}(z,t)$ and $\tau^y_{turb} = \tau^y_{turb}(z,t)$ represent vertical stress for the horizontal components of momentum associated with wind-induced

turbulence in the surface mixed layer. The present study assumes that the turbulent stress has a linear vertical profile at depths in the surface mixed layer and vanishes underneath (Figure S1a in the supporting information),

$$\tau^x_{turb} = \tau^x_{wind} S, \tag{3a}$$

$$\tau^y_{turb} = \tau^y_{wind} S, \tag{3b}$$

$$S = S(z) = \begin{cases} z/H_{mix} + 1 & \text{for} -H_{mix} \le z \le 0, \\ 0 & \text{for} -H_{bottom} \le z < -H_{mix}, \end{cases} \tag{3c}$$

where the sea surface is located at $z = 0$. The symbols H_{mix} and H_{bottom} are the mixed-layer depth and the water depth, respectively, both of which have been assumed to be reference constants in the present study. The symbols $\tau^x_{wind} = \tau^x_{wind}(t)$ in (3a) and $\tau^y_{wind} = \tau^y_{wind}(t)$ in (3b) represent the zonal and meridional components of wind stress applied at the sea surface, respectively. The vertical divergence of the turbulent stress acts as a body force in the momentum equations (2a) and (2b), which has a stepped vertical profile in the present study (Figure S1b). Namely, both the zonal and meridional components of the wind-induced force are vertically constant (τ^x_{wind}/H_{mix} and τ^y_{wind}/H_{mix}, respectively) at depths in the surface mixed layer and vanish underneath. To be useful later in this section, we take the depth integral of the zonal and meridional components of the wind-induced force (i.e., the vertical divergence of the turbulent stress) to yield

$$\int_{-H_{bottom}}^{0} \partial_z\left(\tau^x_{turb}\right) dz = \left(\tau^x_{wind}/H_{mix}\right) H_{mix} = \tau^x_{wind}, \tag{4a}$$

$$\int_{-H_{bottom}}^{0} \partial_z\left(\tau^y_{turb}\right) dz = \left(\tau^y_{wind}/H_{mix}\right) H_{mix} = \tau^y_{wind}. \tag{4b}$$

Likewise, we take the depth integral of the square of each of the zonal and meridional components of the wind-induced force to yield

$$\int_{-H_{bottom}}^{0} \left(\partial_z\left(\tau^x_{turb}\right)\right)^2 dz = \left(\tau^x_{wind}/H_{mix}\right)^2 H_{mix} = \left(\tau^x_{wind}\right)^2/H_{mix}, \tag{5a}$$

$$\int_{-H_{bottom}}^{0} \left(\partial_z\left(\tau^y_{turb}\right)\right)^2 dz = \left(\tau^y_{wind}/H_{mix}\right)^2 H_{mix} = \left(\tau^y_{wind}\right)^2/H_{mix}. \tag{5b}$$

We shall decompose the wind-induced force, mentioned above, to baroclinic normal modes. Let $F^{(n)} = F^{(n)}(z)$ and n be the eigenfunction and its order of the Sturm-Liouville problem associated with the vertical profile of buoyancy frequency $N = N(z)$ in the ocean to read,

$$\partial_z\left(\left(\partial_z F^{(n)}\right)/N^2\right) = -F^{(n)}/\left(c^{(n)}\right)^2, \tag{6a}$$

$$\int_{-H_{bottom}}^{0} \left(F^{(n)}\right)^2 dz = H_{bottom}, \tag{6b}$$

$$\partial_z F^{(n)} = 0 \text{ and } F^{(n)} > 0 \text{ at } z = 0, \tag{6c}$$

$$F^{(n)} = 0 \text{ at } z = -H_{bottom}, \tag{6d}$$

where $c^{(n)}$ is the speed of nonrotating gravity waves for the nth baroclinic mode. The wind-induced force (i.e., the vertical divergence of the turbulent stress) may be decomposed using a set of nondimensional coefficients $\alpha^{(n)}$ associated with the nth baroclinic mode to read,

$$\partial_z\left(\tau^x_{turb}\right) = A^x \textstyle\sum_n \alpha^{(n)} F^{(n)}, \tag{7a}$$

$$\partial_z\left(\tau^y_{turb}\right) = A^y \textstyle\sum_n \alpha^{(n)} F^{(n)}, \tag{7b}$$

$$\textstyle\sum_n \alpha^{(n)2} = 1, \tag{7c}$$

where the symbols $A^x = A^x(t)$ and $A^y = A^y(t)$ represent mode-independent amplitudes associated with the zonal and meridional directions. Using (6a)–(6d) and (7a)–(7c), we revisit the depth integral of the square of each of the zonal and meridional components of the wind-induced force to yield,

$$\int_{-H_{bottom}}^{0}\left(\partial_z\left(\tau^x_{turb}\right)\right)^2 dz = (A^x)^2 H_{bottom}\left(\sum_n \alpha^{(n)2}\right) = (A^x)^2 H_{bottom}, \tag{8a}$$

$$\int_{-H_{bottom}}^{0}\left(\partial_z\left(\tau^y_{turb}\right)\right)^2 dz = (A^y)^2 H_{bottom}\left(\sum_n \alpha^{(n)2}\right) = (A^y)^2 H_{bottom}. \tag{8b}$$

The set of (5a) and (5b) and (8a) and (8b) determines an analytical expression for the mode-independent amplitudes as follows,

$$A^x = \tau^x_{wind}/\sqrt{H_{mix}H_{bottom}}, \tag{9a}$$

$$A^y = \tau^y_{wind}/\sqrt{H_{mix}H_{bottom}}. \tag{9b}$$

We now project the vertical profile of the wind-induced force based on (7a) and (7b) to the eigenfunction of each baroclinic mode to read,

$$\int_{-H_{bottom}}^{0}\left(\partial_z\left(\tau^x_{turb}\right)\right)F^{(n)}dz = A^x H_{bottom}\alpha^{(n)} = \tau^x_{wind}\sqrt{H_{bottom}/H_{mix}}\,\alpha^{(n)}, \tag{10a}$$

$$\int_{-H_{bottom}}^{0}\left(\partial_z\left(\tau^y_{turb}\right)\right)F^{(n)}dz = A^y H_{bottom}\alpha^{(n)} = \tau^x_{wind}\sqrt{H_{bottom}/H_{mix}}\,\alpha^{(n)}, \tag{10b}$$

where (6b) and (9a) and (9b) have been used. Substitution of (3a)–(3c) to (10a) and (10b) yields an analytical expression for the nondimensional coefficient $\alpha^{(n)}$ to read,

$$\alpha^{(n)} = \int_{-H_{mix}}^{0} F^{(n)}dz/\sqrt{H_{bottom}H_{mix}}, \tag{11}$$

which has been estimated in the present study using the set of eigenfunctions associated with the climatological annual mean stratification of the tropical IO (see Figure S1c) to yield 0.35, 0.44, and 0.27 for the first, second, third baroclinic modes, respectively, as listed in Table S1.

Appendix B: Comparison of Observed and Simulated Monsoon Circulations

SM01 (see their Figures 8 and 9 schematic representation of identified current branches during the southwest monsoon and the northeast monsoon, respectively) present a review of monsoon circulation in the IO. During the boreal winter monsoon, northeasterly winds in the Arabian Sea and the Bay of Bengal induce the North Monsoon Current, which flows westward and feeds a southward flow called the SC along the African coasts. This southward flowing boundary current meets the northward flowing EACC in equatorial regions around 2–4°S. Currents from both hemispheres converge and furnish the South Equatorial Counter Current that flows eastward along the equator [Düing & Schott, 1978; Swallow et al., 1991; SM01; Beal et al., 2013]. During the boreal summer monsoon, southwesterly winds in the Arabian Sea induce a strong northward EACC that originates from the South Equatorial Current along the African coasts. As the EACC crosses the equator, a portion of it turns offshore and starts to flow eastward at about 4°N toward the Bay of Bengal [SM01; Nagura & Masumoto, 2015]. Along the Australian coastline, signals from the Indonesian Throughflow region travel poleward as RWs are radiated into the southern IO (Cai et al., 2005). This latter mechanism represents an important means of energy transmission from the Pacific Ocean to the IO.

The horizontal distributions of experimental results for the second baroclinic mode (Figure S2 in the supporting information) illustrate the annual variations taking place in the IO. The model results reproduce the Somali jet along the African coasts. The variations of the Somali jet are related to the interactions in the tropical-extratropical IO. The results also illustrate how a large-scale monsoon leads to the formation of the Somali jet. In boreal winter along the African coasts (Figure S2a), the southward signals of the SC originate from the North Monsoon Current while the northward signals of the EACC originate from the South Equatorial Current [SM01; Schott, 1986; Nagura & Masumoto, 2015]. These equatorward boundary currents

meet each other around the equator to turn eastward as the South Equatorial Counter Current (Düing & Schott, 1978; Swallow et al., 1991), in such a way as to relax negative geopotential anomaly in the western equatorial region (Figure S2b). With the onset of the boreal summer monsoon, southwesterly winds induce a strong northward EACC flowing along the African coasts (Figure S2e). As this crosses the equator, it turns offshore and starts to flow eastward toward the Arabian Sea. The southwesterly winds give rise to coastal upwelling near the African coasts, as shown by negative geopotential anomaly in Figure S2f. These results demonstrate that several of the basic features of the climatological circulation and wave evolution in the IO have been captured by our model experiments.

Appendix C: Schemes for Calculating the Group Velocity-Based Energy Flux

Here we explain three schemes that have been proposed for diagnosing the group velocity-based transfer routes of wave energy. Wave energy $E^{(n)}$ for the nth baroclinic mode may be defined as

$$E^{(n)} \equiv \rho_0 \left[u^{(n)2} + v^{(n)2} + \left(p^{(n)}/c^{(n)} \right)^2 \right] /2, \tag{12a}$$

where $u^{(n)}$ and $v^{(n)}$ indicate the zonal and meridional components of velocity, respectively, and $p^{(n)}$ is geopotential. The symbols ρ_0 and $c^{(n)}$ are constants for the reference density of seawater and nonrotating gravity wave speed, respectively. An equation for the development of wave energy may be derived using (1a)–(1c) to yield

$$\partial_t \overline{E^{(n)}} + \rho_0 \nabla \cdot \ll \overline{u^{(n)} p^{(n)}}, \overline{v^{(n)} p^{(n)}} \gg = S_{in} \quad + \quad S_{dis}, \tag{12b}$$

where $\nabla \cdot \ll A,B \gg = \partial_x A + \partial_y B$ is the horizontal divergence operator (A and B are arbitrary quantities). The overbar denotes a phase average. The horizontal coordinates x and y increase eastward and northward, respectively. Energy input by wind forcing (Figure 3e) is written as

$$S_{in} = \frac{\alpha^{(n)}}{\sqrt{H_{mix} H_{bottom}}} \left(\overline{u^{(n)} \tau^x_{wind}} + \overline{v^{(n)} \tau^y_{wind}} \right), \tag{12c}$$

where wind stress vector $(\tau^x_{wind}, \tau^y_{wind})$ is the seasonal anomaly component of monthly climatology between September 1957 and August 2002. Energy dissipation is written as

$$S_{dis} = \rho_0 \left(\overline{u^{(n)} SGS^x} + \overline{v^{(n)} SGS^y} \right), \tag{12d}$$

where the SGS terms in (12d) represent the effect of lateral eddy viscosity based on the Smagorinsky et al. (1965) scheme with a nondimensional coefficient of 0.1 after squaring. In our model, the SGS terms have been expressed as

$$SGS^x = \partial_x \left[\kappa \left(2u^{(n)}_x \right) \right] + \partial_y \left[\kappa \left(u^{(n)}_y + v^{(n)}_x \right) \right], \tag{12e}$$

$$SGS^y = \partial_x \left[\kappa \left(u^{(n)}_y + v^{(n)}_x \right) \right] + \partial_y \left[\kappa \left(2v^{(n)}_y \right) \right], \tag{12f}$$

where κ is the coefficient of lateral eddy viscosity. Substitution of (12e) and (12f) to (12d) yields

$$S_{dis} = S_{dis:div} + S_{dis:nd}, \tag{12g}$$

$$S_{dis:div} = \rho_0 \partial_x \left[\overline{2\kappa u^{(n)} \left(u^{(n)}_x \right) + \kappa v^{(n)} \left(u^{(n)}_y + v^{(n)}_x \right)} \right] + \rho_0 \partial_y \left[\overline{\kappa u^{(n)} \left(u^{(n)}_y + v^{(n)}_x \right) + 2\kappa v^{(n)} \left(v^{(n)}_y \right)} \right], \tag{12h}$$

$$S_{dis:nd} = -\rho_0 \overline{\kappa \left[2 \left(u^{(n)}_x \right)^2 + \left(u^{(n)}_y + v^{(n)}_x \right)^2 + 2 \left(v^{(n)}_y \right)^2 \right]}, \tag{12i}$$

where the dissipation term has been separated into the divergent and negative-definite parts. Figure 3f shows the distribution of the negative-definite part.

The expression of energy flux in (12b) may be referred to as pressure flux scheme

$$\ll \overline{u^{(n)}p^{(n)}}, \overline{v^{(n)}p^{(n)}} \gg. \tag{13}$$

If applied to the diagnosis of inertia-gravity waves, the pressure flux becomes identical to group velocity times wave energy (Cummins & Oey, 1997). The results of calculating the pressure flux are shown in Figures 2a and 2b. The pressure flux scheme cannot represent the direction of group velocity for midlatitude RWs.

Without affecting the result of the divergence in the energy budget equation (12b), one may add a rotational flux to read

$$\ll \overline{u^{(n)}p^{(n)}} + \left[\overline{p^{(n)2}}/(2f)\right]_y, \overline{v^{(n)}p^{(n)}} - \left[\overline{p^{(n)2}}/(2f)\right]_x \gg, \tag{14}$$

which becomes identical to group velocity times wave energy for midlatitude RWs.

The expression of the energy flux in (14) is referred to as OS93 scheme. The OS93 scheme becomes singular at the equator owing to the Coriolis parameter in the denominator. The results of calculating the OS93 flux are shown in Figures 2c and 2d.

AGC17 have derived a seamless expression for the energy flux that can represent the direction of group velocity for both gravity and planetary waves at all latitudes. What they call the level-0 (i.e. exact) version of the AGC energy flux may be written as

$$\ll \overline{u^{(n)}p^{(n)}} + \left(\overline{p^{(n)}\varphi^{(n)}}/2 + \overline{u_{tt}^{(n)}\varphi^{(n)}}/\beta\right)_y, \overline{v^{(n)}p^{(n)}} - \left(\overline{p^{(n)}\varphi^{(n)}}/2 + \overline{u_{tt}^{(n)}\varphi^{(n)}}/\beta\right)_x \gg, \tag{15a}$$

where β is the meridional gradient of the Coriolis parameter. The scalar quantity $\varphi^{(n)}$ is given by solving an inversion equation associated with Ertel's potential vorticity to read

$$\nabla^2\varphi^{(n)} - \left(f/c^{(n)}\right)^2\varphi^{(n)} - \left(3/c^{(n)2}\right)\varphi_{tt}^{(n)} = q^{(n)}, \tag{15b}$$

$$q^{(n)} \equiv v_x^{(n)} - u_y^{(n)} - \left(f/c^{(n)2}\right)p^{(n)}, \tag{15c}$$

where $\nabla^2 = \partial_{xx} + \partial_{yy}$.

Inversion equation (15b) contains a second-order time derivative term associated with $\varphi_{tt}^{(n)}$, which makes it difficult to get the solution of $\varphi^{(n)}$. AGC17 have presented an approximated version of the energy flux to read,

$$\ll \overline{u^{(n)}p^{(n)}} + \left(\overline{p^{(n)}\varphi^{app}}/2\right)_y, \overline{v^{(n)}p^{(n)}} - \left(\overline{p^{(n)}\varphi^{app}}/2\right)_x \gg, \tag{16a}$$

$$\nabla^2\varphi^{app} - \left(f/c^{(n)}\right)^2\varphi^{app} = q^{(n)}, \tag{16b}$$

which has been referred to as Level-2 expression. The results of calculating the AGC17 Level-2 flux are shown in Figures 2e, 2f, 3a–3c, and 4. AGC17 have suggested that the quantity φ^{app} reduces to geostrophic stream function in off-equatorial regions (see contours in the right panels of Figure S2 in the supporting information).

We consider the Helmholtz decomposition of the AGC17 Level-2 flux to read,

$$-R_y - D_x = \rho_0\overline{u^{(n)}p^{(n)}} + \rho_0\left(\overline{p^{(n)}\varphi^{app}}/2\right)_y, \tag{17a}$$

$$+R_x - D_y = \rho_0\overline{v^{(n)}p^{(n)}} - \rho_0\left(\overline{p^{(n)}\varphi^{app}}/2\right)_x, \tag{17b}$$

where the scalar quantities R and D are associated with the rotational and divergent components of the energy flux, respectively, and have a unit of W/m. Taking the curl of (17a) and (17b) yields

$$\nabla^2 R = \rho_0 \left(\overline{v^{(n)} p^{(n)}}\right)_x - \rho_0 \left(\overline{u^{(n)} p^{(n)}}\right)_y - \rho_0 \nabla^2 \left(\overline{p^{(n)} \varphi^{app}}/2\right), \tag{17c}$$

which has been numerically solved to obtain the distribution of R as shown by color shading in Figure 3c. Taking the convergence of (17a) and (17b) yields

$$\nabla^2 D = -\rho_0 \left(\overline{u^{(n)} p^{(n)}}\right)_x - \rho_0 \left(\overline{v^{(n)} p^{(n)}}\right)_y, \tag{17d}$$

which has been numerically solved to obtain the distribution of D as shown by contours in Figure 3d. The scalar quantities R and D may be referred to as energy flux stream function and energy flux potential, respectively.

Acknowledgments
This manuscript has been improved by insightful comments from three anonymous reviewers. The set of model outputs obtained during the last year of each of the three experiments performed in the present study will be archived at both https://www.diasjp.net/en/ and http://cidas.isee.nagoya-u.ac.jp/databases/index.shtml.en upon publication of this manuscript. A number of data sets were retrieved from the Asia-Pacific Data Research Center at the University of Hawai'i (http://apdrc.soest.hawaii.edu). These include temperature and salinity data from the World Ocean Atlas 2013 for the calculation of gravity wave phase speed, mixed-layer depth data from the Argo products, and wind velocity data from the European Centre for Medium-Range Weather Forecasts Re-analysis (ECMWF ERA-40) for estimation of climatological wind forcing. The authors thank Yoshiki Fukutomi, Tomomichi Ogata, and Qingyang Song for helpful discussions. This study was supported by Japan Society for the Promotion of Science KAKENHI Grants 18H03738 and 15H02129.

References

Aiki, H., Greatbatch, R. J., & Claus, M. (2017). Towards a seamlessly diagnosable expression for the energy flux associated with both equatorial and mid-latitude waves. *Progress in Earth and Planetary Science*, *4*(1), 11. https://doi.org/10.1186/s40645-017-0121-1

Beal, L., Hormann, V., Lumpkin, R., & Foltz, G. (2013). The response of the surface circulation of the Arabian Sea to monsoonal forcing. *Journal of Physical Oceanography*, *43*(9), 2008–2022. https://doi.org/10.1175/JPO-D-13-033.1

Cai, W., Meyers, G., & Shi, G. (2005). Transmission of ENSO signal to the Indian Ocean. *Geophysical Research Letters*, *32*, L05616. https://doi.org/10.1029/2004GL021736

Cummins, P. F., & Oey, L. Y. (1997). Simulation of barotropic and baroclinic tides off northern British Columbia. *Journal of Physical Oceanography*, *27*, 762–781. https://doi.org/10.1175/1520-0485(1997)027<0762:SOBABT>2.0.CO;2

Düing, W., & Schott, F. (1978). Measurements in the source region of the Somali current during the monsoon reversal. *Journal of Physical Oceanography*, *8*, 278–289. https://doi.org/10.1175/1520-0485(1978)008<0278:MITSRO>2.0.CO;2

Fukutomi, Y., & Yasunari, T. (2002). Tropical-extratropical interaction associated with the 10–25-day oscillation over the western Pacific during the northern summer. *Journal of the Meteorological Society of Japan*, *80*, 311–331. https://doi.org/10.2151/jmsj.80.311

Gent, P. R., O'Neill, K., & Cane, M. A. (1983). A model of the semiannual oscillation in the equatorial Indian Ocean. *Journal of Physical Oceanography*, *13*(12), 2148–2160. https://doi.org/10.1175/1520-0485(1983)013<2148:AMOTSO>2.0.CO;2

Huang, B., & Kinter, J. L. (2002). Interannual variability in the tropical Indian Ocean. *Journal of Geophysical Research*, *107*(C11), 3199. https://doi.org/10.1029/2001JC001278

Large, W. G., & Pond, S. (1981). Open ocean momentum flux measurements in moderate to strong winds. *Journal of Physical Oceanography*, *11*, 324–336. https://doi.org/10.1175/1520-0485(1981)011<0324:OOMFMI>2.0.CO;2

Mark, R. J., & Huang, B. (2004). The Rossby wave as a key mechanism of Indian Ocean climate variability. *Deep Sea Research, Part I*, *51*, 2123–2136. https://doi.org/10.1016/j.dsr.2004.06.005

McPhaden, M. J., & Ripa, P. (1990). Wave-mean flow interactions in the equatorial ocean. *Annual Review of Fluid Mechanics*, *20*, 167–205. https://doi.org/10.1146/annurev.fl.22.010190.001123

Nagura, M., & Masumoto, Y. (2015). A wake due to the Maldives in the eastward Wyrtki jet. *Journal of Physical Oceanography*, *45*(7), 1858–1876. https://doi.org/10.1175/JPO-D-14-0191.1

Nagura, M., & McPhaden, M. J. (2010). Wyrtki Jet dynamics: Seasonal variability. *Journal of Geophysical Research*, *115*, C07009. https://doi.org/10.1029/2009JC005922

Ogata, T., & Aiki, H. (2019). The pathway of intraseasonal wave energy in the tropical Indian Ocean as identified by a seamless diagnostic scheme. *Scientific Online Letters on the Atmosphere*, *15*, 262–267. https://doi.org/10.2151/sola.2019-047

Ogata, T., Nagura, M., & Masumoto, M. (2017). Mean subsurface upwelling induced by intraseasonal variability over the equatorial Indian Ocean. *Journal of Physical Oceanography*, *47*, 1347–1365. https://doi.org/10.1175/JPO-D-16-0257.1

Orlanski, I., & Sheldon, J. (1993). A case of downstream baroclinic development over western north America. *Monthly Weather Review*, *121*, 2929–2950. https://doi.org/10.1175/1520-0493(1993)121<2929:ACODBD>2.0.CO;2

Rahul, P. C. R., Salvekar, P. S., Deo, A. A., & Ganer, D. W. (2004). Westward propagating twin gyres in the equatorial Indian Ocean. *Geophysical Research Letters*, *31*, L01304. https://doi.org/10.1029/2003GL018615

Rao, R. R., Girish Kumar, M. S., Ravichandran, M., Rao, A. R., Gopalakrishna, V. V., & Thadathil, P. (2010). Interannual variability of Kelvin wave propagation in the wave guides of the equatorial Indian Ocean, the coastal Bay of Bengal and the southeastern Arabian Sea during 1993–2006. *Deep Sea Research, Part I*, *57*, 1–13. https://doi.org/10.1016/j.dsr.2009.10.008

Rao, S. A., & Yamagata, T. (2004). Abrupt termination of Indian Ocean dipole events in response to intra-seasonal oscillations. *Geophysical Research Letters*, *31*, L19306. https://doi.org/10.1029/2004GL020842

Saji, N. H., Goswami, B. N., Vinayachandran, P. N., & Yamagata, T. (1999). A dipole in the tropical Indian Ocean. *Nature*, *401*, 360–363. https://doi.org/10.1038/43854

Schopf, P. S., Anderson, D. L. T., & Smith, R. (1981). Beta-dispersion of low-frequency Rossby waves. *Dynamics of Atmospheres and Oceans*, *5*, 187–214. https://doi.org/10.1016/0377-0265(81)90011-7

Schott, F. (1986). Seasonal variation of cross-equatorial flow in the Somali Current. *Journal of Geophysical Research*, *91*, 10,581–10,584. https://doi.org/10.1029/JC091iC09p10581

Schott, F. A., & McCreary, J. P. (2001). The monsoon circulation of the Indian Ocean. *Progress in Oceanography*, *51*, 1–123. https://doi.org/10.1016/S0079-6611(01)00083-0

Smagorinsky, J., Manabe, S., & Holloway, J. L. (1965). Numerical results from a nine-level general circulation model of the atmosphere. *Monthly Weather Review*, *93*, 727–768. https://doi.org/10.1175/1520-0493(1965)093<0727:NRFANL>2.3.CO;2

Swallow, J. C., Schott, F., & Fieux, M. (1991). Structure and transport of the East African Coastal Current. *Journal of Geophysical Research*, *96*, 22,254–22,267. https://doi.org/10.1029/91JC01942

Tailleux, R., & McWilliams, J. C. (2001). The effect of bottom pressure decoupling on the speed of extratropical, baroclinic Rossby waves. *Journal of Physical Oceanography*, *31*, 1461–1476. https://doi.org/10.1175/1520-0485(2001)031<1461:TEOBPD>2.0.CO;2

Ummenhofer, C. C., Biastoch, A., & Böning, C. W. (2017). Multidecadal Indian Ocean variability to the Pacific and implications for preconditioning Indian Ocean dipole events. *Journal of Climate*, *30*(5), 1739–1751. https://doi.org/10.1175/JCLI-D-16-0200.1

Wyrtki, K. (1973). An equatorial jet in the Indian Ocean. *Science*, *181*, 262–264. https://doi.org/10.1126/science.181.4096.262

Yanai, M., & Maruyama, T. (1966). Stratospheric wave disturbances propagating over the equatorial pacific. *Journal of the Meteorological Society of Japan*, *44*, 291–294. https://doi.org/10.2151/jmsj1965.44.5_291

Yu, L., O'Brien, J. J., & Yang, J. (1991). On the remote forcing of the circulation in the Bay of Bengal. *Journal of Geophysical Research*, *96*(C11), 20,449–20,454. https://doi.org/10.1029/91JC02424